

Modeling emission of acoustic energy during bubble expansion in PICO bubble chambers

Tetiana Kozynets,^{1,*} Scott Fallows,¹ and Carsten B. Krauss¹

¹*Department of Physics, University of Alberta, Edmonton, T6G 2E1, Canada*

(Dated: June 11, 2019)

The PICO experiment uses bubble chambers filled with superheated C_3F_8 for spin-dependent WIMP dark matter searches. One of the main sources of background in these detectors is alpha particles from decays of environmental ^{222}Rn , which nucleate bubbles that are visually indistinguishable from WIMP candidate events. Alpha-induced bubbles can be discriminated acoustically, because the signal from alpha events is consistently larger in magnitude than that from nuclear recoil/WIMP-like events. By studying the dynamics of bubbles nucleated by these two types of ionizing radiation from the first stages of their growth, we present a physical model for the acoustic discrimination for the first time. The distribution of acoustic energies that we generate for a simulated sample of bubble nucleations by alpha particles and nuclear recoils is compared directly to the experimental data.

I. INTRODUCTION

Bubble chambers played an important role in experimental advances of particle physics in the 1950s and 1960s [1]. Initially, they were operated at very high superheats to allow reliable bubble nucleation by minimally ionizing particles. Over the last decade bubble chambers have made a resurgence in dark matter searches, where the chambers are operated at more moderate superheats that explicitly prevent nucleation from minimally ionizing particles. This way, the chambers are only sensitive to nuclear recoils and other highly ionizing particle interactions.

The PICO experiment searches for WIMP dark matter candidates using bubble chamber technology [2–4]. To calibrate the detector, neutron radiation from a source of known activity, typically ^{252}Cf or $^{241}\text{Am}/^{9}\text{Be}$, is used. Neutron source calibrations allow the observation of nuclear recoil events in the range of keV recoil energies, creating an acoustic signature that is identical to the expected recoil signal from dark matter interactions.

Alpha radiation from decays of environmental ^{222}Rn is one of the dominant sources of background. Visually, bubbles nucleated by α particles are indistinguishable from nuclear recoil/WIMP-like events. It was discovered in the PICASSO experiment that the acoustic signature of a nucleation from an α event is more powerful than the acoustic signal of a nuclear recoil event [5]. So far this has been explained with a model that lacked specific predictability. To reveal the origin of the observed differences in acoustic signal magnitudes, we connect the initial thermodynamic conditions of bubble nucleation by α particles and nuclear recoils with the specifics of bubble evolution. We approach this problem with a molecular dynamics simulation, which lets us vary the energy deposited by an incident ion and the shape of the initially vaporized region to reproduce α -like and nuclear recoil-like scenarios. We further study the influence of these variables on the dynamics of a nucleated nonspherical

bubble and analytically link the first expansion stages to the well-described spherical bubble growth [6, 7]. Finally, we reconstruct the acoustic pressure signal from the spherical bubble growth histories for both α -induced and nuclear recoil-induced bubbles. The results of the developed model are compared to recent acoustic data from the PICO-60 detector [2, 3], which used superheated C_3F_8 as the target fluid.

II. INPUTS TO THE ACOUSTIC EMISSION MODEL

A. Molecular dynamics (MD) simulations

To model the nucleation and subsequent expansion of bubbles in superheated C_3F_8 , we make use of the Large-Scale Atomic/Molecular Massively Parallel Simulator (LAMMPS) [8]. Inside this package, we represent C_3F_8 as a system of atoms interacting according to the Lennard-Jones (LJ) potential with characteristic energy ϵ and characteristic distance σ (see Appendix A for details). This method neglects interatomic interactions within the molecules themselves, following the approach of [9] to model C_2ClF_5 used in the SIMPLE experiment [10]. The Lennard-Jones potential description of any fluid is complete when the ϵ and σ parameters are specified. Setting $\epsilon = 0.0318\text{ eV}$ makes the critical temperature of an LJ fluid match that of C_3F_8 . We also aim to simulate the specific conditions of the PICO-60 run at temperature $T_0 \simeq 14^\circ\text{C}$ and liquid pressure $P_1 \simeq 207\text{ kPa}$ (30 psi). This corresponds to the C_3F_8 liquid density of $\rho_1 = 1379\text{ kg m}^{-3}$, which we can reproduce with $\sigma = 0.533\text{ nm}$. At 14°C , such a choice results in a 16% discrepancy between the REFPROP [11] value of equilibrium pressure at saturation and the Lennard-Jones value measured from our MD simulations; 33% between REFPROP-extracted and simulated vapor densities; and 25% between the surface tension values. Appendix A summarizes the steps we took to arrive at these results.

To bring the LJ fluid approximating C_3F_8 to the speci-

* kozynets@ualberta.ca

fied superheated state, we follow the procedure described in [9] and outlined in [Appendix B](#). As in [9], we proceed with simulating the heat spike by depositing energy E_{dep} within a narrow and long cylindrical region in the metastable liquid, mimicking the track of an ionizing particle. According to the Seitz model [12], a minimum of \mathcal{T}_{\min} must be deposited along $l_{\text{cyl}} = 2R_c$ for the nucleated bubble to surpass its critical radius R_c and continue growing stably. To imitate nuclear recoils, we perform several simulations with l_{cyl} equal to integer multiples of R_c ($40.58\sigma \approx 21.63 \text{ nm}$ at our conditions) and energy deposits close to \mathcal{T}_{\min} . The radius of the cylindrical energy deposition region is fixed at $r_{\text{cyl}} = 2\sigma \approx 1.066 \text{ nm}$. To simulate α -like bubble nucleations, we deposit energies of order 10 keV along μm -long cylindrical tracks, with $r_{\text{cyl}} = 3\sigma \approx 1.599 \text{ nm}$. We justify these geometry choices in [Appendix B](#).

The simulated bubbles are allowed to grow under *NPT* (constant particle number, pressure, and temperature) constraints through several major stages. These include rapid initial bubble expansion, followed by slight decrease in the bubble volume over a short time interval, and subsequent transition to the inertial growth phase. In this phase, the effective bubble radius R_{eff} increases nearly linearly with time, being controlled by the forces of liquid inertia. When the bubble, which grew out of a long cylindrical vapor region, becomes spherical, we may predict its further behavior by solving the differential equation describing spherical bubble growth [6, 7]. This technique allows us to simulate only the first few tens of nanoseconds of bubble expansion in LAMMPS, feeding the MD-based $R(t)$ history into the familiar expressions for R at later times. In [Sec. IID](#), we show that α -induced bubbles transition from nonspherical to spherical in a similar fashion, meaning that the same approach is applicable to predicting their growth.

B. Post-simulation processing: Bubble surface tracking

From each molecular dynamics simulation, we save 2D distributions of liquid densities in the XY plane running through the middle of the simulation volume (see [Appendix C](#) for details). With energy deposited along the x -axis, the XY plane fully captures the 3D bubble growth, given that the z -axis is physically no different from the y -axis. These density distributions are then used as an input to the marching squares algorithm [13, 14], which allows us to extract the contours of constant density values. As per [Appendix C](#), the longest contour of $\rho_l \approx 830 \text{ kg m}^{-3}$ accurately reproduces the liquid-vapor boundary at each t . The (x, y) coordinates of this boundary let us evaluate the bubble radius as a function of polar angle $\phi \equiv \tan^{-1}(y/x)$. In the present work, we take advantage of this to track the eccentricity of bubbles and thereby define the time elapsed after the heat spike when each bubble can be considered nearly spherical. As discussed in [Sec. IIC](#),

specifying this time and the corresponding value of the bubble radius makes for an initial condition sufficient to predict the subsequent bubble evolution. In [Fig. 1](#), we give an example of bubble boundary extraction results at several representative times after the heat spike.

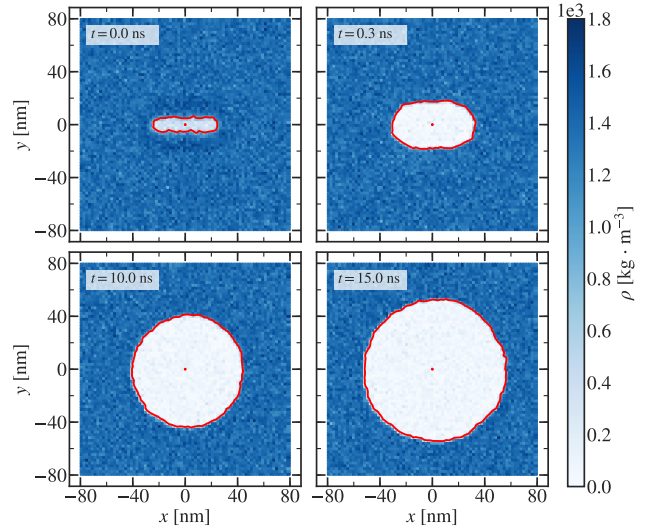


FIG. 1. Example time evolution of a simulated bubble (this case: $E_{\text{dep}} = 3.75 \text{ keV}$ deposited along $l_{\text{cyl}} = 2R_c$, parallel to the x -axis). The plots show positions of the grid cells in the XY plane, color-coded by the time-averaged fluid densities in the cells. The solid red line is the longest contour extracted with the marching squares algorithm [13, 14] from the density data, defining the bubble surface boundary in each case.

C. Predicting evolution of a spherical bubble in the linear and thermal growth phases

Molecular dynamics simulations, even for liquid volumes as small as those considered so far, are quite computationally expensive: for instance, $\sim 1 \text{ ns}$ of a typical bubble evolution in an *NPT* ensemble takes about 720 CPU-hours to run in LAMMPS. At the same time, radiation of acoustic energy as the result of bubble growth spans much longer time scales. These are roughly defined by the time of transition from the inertial bubble growth phase to the thermal growth phase, which features much slower expansion and consequently smaller amplitudes of the emitted sound waves [15]. For a bubble growing in superheated C_3F_8 , the characteristic inertial growth phase duration is of order $100 \mu\text{s}$ [4]. This makes simulating the whole acoustic emission practically impossible with molecular dynamics methods alone. Such a complication calls for a way to fully predict bubble evolution based on a short history of its growth. The method has to be further generalized to the case of an arbitrary energy deposition, letting us perform MD simulations for only a few different E_{dep} values and extrapolate the results to other energies.

To proceed, we need to make a connection between bubble nucleation conditions, growth of the resulting

highly nonspherical bubbles, and well-described spherical bubble dynamics. By combining the Rayleigh-Plesset equation [7] for the inertial growth phase and the Plesset-Zwick equation [6] for the thermal growth phase as in [16], we arrive at the bubble growth rate

$$\frac{dR}{dt} = - \left[\frac{A^2 \sqrt{t - t_s}}{B} + \frac{2\nu_l}{R} \right] + \sqrt{A^2 - \frac{2\gamma}{\rho_l R} + \left(\frac{2\nu_l}{R} + \frac{A^2 \sqrt{t - t_s}}{B} \right)^2}. \quad (1)$$

In Eq. 1, the constant A is a characteristic speed of expansion in the inertial phase. It is given by

$$A = \sqrt{\frac{2h\rho_v\Delta T}{3\rho_l T_{\text{sat}}}}, \quad (2)$$

where h is the latent heat of vaporization, ΔT is the liquid superheat above the saturation temperature T_{sat} for a given liquid density ρ_l , and ρ_v is the vapor density inside the bubble. The constant B in (1) may be expressed as

$$B = \sqrt{\frac{12}{\pi a_l}} Ja, \quad (3)$$

where a_l is the thermal diffusivity of the liquid and Ja is its Jakob number ($Ja = \frac{\Delta T c_l \rho_l}{h \rho_v}$, with c_l being the liquid heat capacity.) The other quantities appearing in Eq. 1 are the liquid viscosity ν_l and the surface tension γ , whose contributions are non-negligible for the small bubble sizes simulated in LAMMPS. In Table I, we provide the REFPROP values of these properties for C_3F_8 at 14°C and 207 kPa (30 psia), as well as the A and B constants evaluated according to Eqs. 2 and 3. For our C_3F_8 -like LJ fluid, we may also find A , B , γ , and ν_l by fitting that part of the simulation-extracted $R(t)$ data where the bubble is spherical. To determine when this happens, we examine the time evolution of bubble eccentricity, defined as

$$\tilde{e} = \sqrt{1 - \frac{R_{90}^2}{R_0^2}}, \quad (4)$$

with R_0 being the bubble radius in the direction of energy deposition ($\phi = 0^\circ$) and R_{90} being that in the orthogonal direction ($\phi = 90^\circ$). The bubble eccentricity as a function of time corresponding to $R(t)$ from Fig. 2a is shown in Fig. 2b. We choose to use the first minimum in bubble eccentricity as an approximation for the time t_s required for the bubble to become spherical. Each t_s corresponds to a certain bubble radius value R_s . $R(t_s) = R_s$ serves as the initial condition for Eq. 1, which we fit simultaneously to the four simulated data sets as described in Appendix D. With parameter A fixed at its value predicted for C_3F_8 with Eq. 2, we find a satisfactory agreement between the best-fitting B and γ and their C_3F_8 values (see Table I). The viscosity of C_3F_8 differs from the value we extract

Property	Value	Unit
h : enthalpy of vaporization	82.58	kJ kg^{-1}
c_l : liquid heat capacity	1130.5	$\text{J kg}^{-1} \text{K}^{-1}$
a_l : liquid thermal diffusivity	0.030	$\text{mm}^2 \text{s}^{-1}$
ρ_v : vapor density	59.4	kg m^{-3}
ρ_l : liquid density	1379.0	kg m^{-3}
T_{sat} : saturation temperature	253.57	K
A (Eq. 2)	17.7	m s^{-1}
B (Eq. 3)	0.0036	$\text{m s}^{-1/2}$
	$0.0084 \pm 0.0002^\dagger$	$\text{m s}^{-1/2}$
ν_l : kinematic viscosity	0.141	$\text{mm}^2 \text{s}^{-1}$
	$18.3 \pm 0.4^\dagger$	$\text{mm}^2 \text{s}^{-1}$
γ : surface tension	4.9	mN m^{-1}
	$3.667 \pm 0.007^\dagger$	mN m^{-1}

TABLE I. Select thermodynamic properties of C_3F_8 at 14°C and 207 kPa (30 psia) extracted from REFPROP [11]. When appropriate, we also list the respective values found for the C_3F_8 -like LJ fluid and use a dagger[†] to denote these cases.

for our LJ fluid by more than two orders of magnitude. This is a natural result since the Lennard-Jones potential completely neglects the intramolecular interactions within C_3F_8 and cannot reproduce all of its thermodynamic properties at once.

With all parameters in Eq. 1 determined for our LJ fluid, we can predict the evolution of bubbles nucleated within it for all $t \geq t_s$. In Fig. 3, we give an example of such a prediction for a bubble nucleated from $E_{\text{dep}} = 5 \text{ keV}$ deposited along $l_{\text{cyl}} = 2R_c$. However, it remains to be shown how exactly the initial condition $R(t_s) = R_s$ varies with E_{dep} and l_{cyl} . As per Appendix D, we find

$$t_s \text{ [ns]} \approx (0.082 \pm 0.006) l_{\text{cyl}} \text{ [nm]} \quad (5)$$

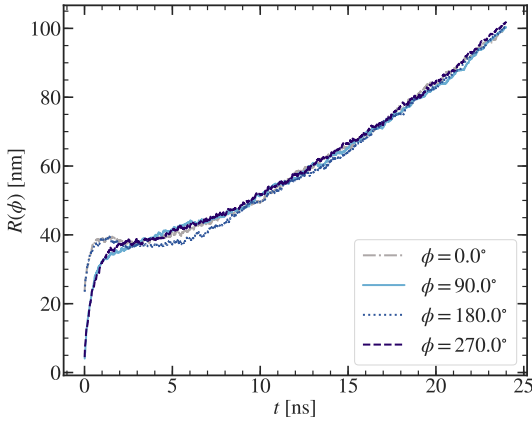
and

$$R_s \text{ [nm]} \approx (0.38 \pm 0.03) l_{\text{cyl}} \text{ [nm]} + (217 \pm 27) \frac{E_{\text{dep}}}{l_{\text{cyl}}} \left[\frac{\text{keV}}{\text{nm}} \right]. \quad (6)$$

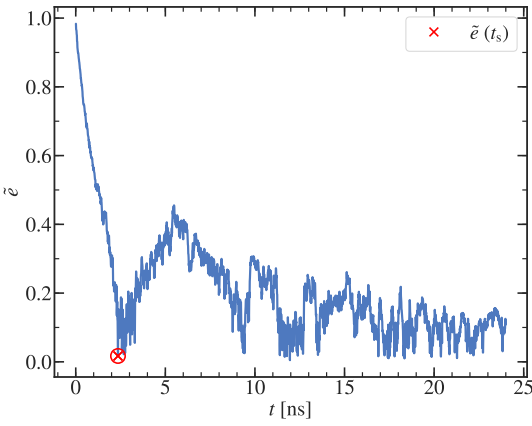
Together, Eqs. 5 and 6 provide the initial condition for Eq. 1 given deposited energies and lengths of ion tracks, which are known for both nuclear recoils and α particles.

D. Predicting the growth of α -induced bubbles

Three populations of alpha-decay events have been observed in the PICO bubble chambers:

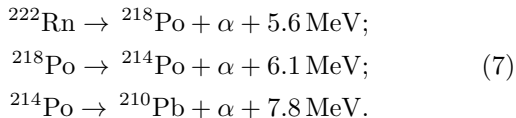


(a) Bubble radius as a function of time elapsed after the simulated energy deposition of 5 keV along $l_{\text{cyl}} = 2R_c \approx 43.3$ nm, extracted at different angles ϕ with the energy deposition direction (see Sec. II B).



(b) Bubble eccentricity (4) derived from the $R(t)$ data in Fig. 2a. The first minimum (the circled red cross) is taken as the definition of time t_s after which the bubble can be treated as spherical.

FIG. 2. The strategy for defining the range of applicability of the spherical bubble growth equation (1) to the evolution of a bubble simulated in the superheated C_3F_8 -like LJ fluid.



These events belong to the decay chain of environmental ^{222}Rn , which creates a background of α particles depositing their energy within the superheated C_3F_8 . Once bubbles nucleated as the result of such an energy deposition grow to a visible size, they cannot be distinguished from neutron-induced bubbles based on visual appearance. Instead, the acoustic parameter (AP) has been introduced as a measure of acoustic energy radiated during bubble expansion [2]. AP provides excellent

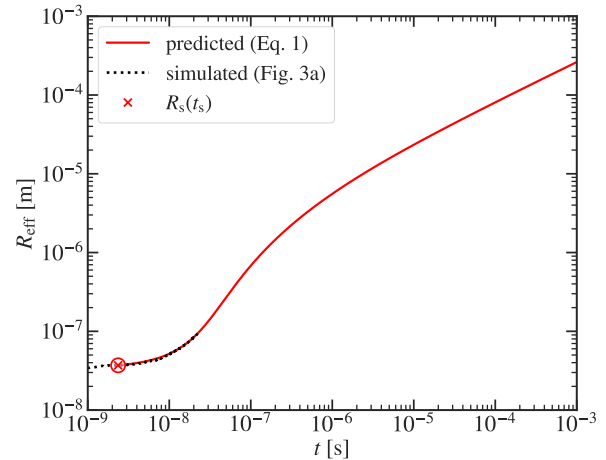


FIG. 3. Time evolution of effective bubble radius R_{eff} for a bubble nucleated from the energy deposition of $E_{\text{dep}} = 5$ keV over $l_{\text{cyl}} = 2R_c \approx 43.3$ nm. We show the bubble growth history extracted from LAMMPS (dotted black line) and that predicted with Eq. 1 (solid red line), with the red cross denoting the moment when the bubble became spherical.

discrimination against α -induced bubbles, which are consistently 5-10 times louder than those from nuclear recoils. One of the hypotheses proposed to explain this was that α particles, with depths of penetration into C_3F_8 of order 10 μm , create several protobubbles along their track. This was contrasted with a single-bubble event typically occurring as the result of a nuclear recoil. The hypothesized protobubbles were assumed to grow and radiate sound independently, further merging into a single large bubble. It was shown in [9] that multiple bubbles are indeed formed when $E_{\text{dep}} \simeq 812.5$ eV is deposited along a 162 nm long track, which corresponds to $\frac{dE}{dx} \simeq 5 \frac{\text{keV}}{\mu\text{m}}$. This value is far below the energies that ^{222}Rn chain α particles deposit within C_3F_8 per unit length; in Fig. 4, we plot $\frac{dE}{dx}$ lost to ionization as a function of α penetration depth in C_3F_8 of $\rho_1 = 1379 \text{ kg m}^{-3}$. These data are extracted with the Stopping Range of Ions in Matter (SRIM) package [17] for α particles with energies equal to the full energies released in the decays. Thus, we approximate the energy deposition by an α particle and a corresponding recoiling nucleus as that by an α only. Given that recoil energies for the heavy nuclei in Eq. 7 are of 100 keV order, such an approximation introduces less than 2% error. From Fig. 4, we then observe that the smallest energy deposition per unit length to the left of the Bragg peak is nearly 75 $\frac{\text{keV}}{\mu\text{m}}$ for the most energetic α , exceeding the energy deposition attempted in [9] by an order of magnitude. Therefore, we need to explicitly consider the cases of 5.6, 6.1, and 7.8 MeV α particles in terms of feasibility of the protobubble formation scenario. The specific thermodynamic conditions of the target liquid must likewise be taken into account.

To perform the necessary checks, we simulate 10, 30,

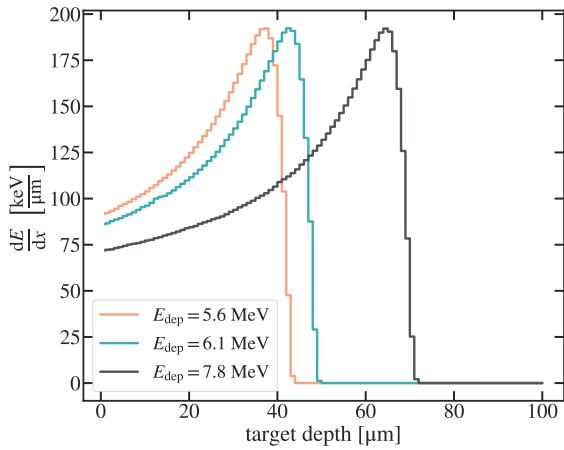


FIG. 4. Energy per unit length lost by α particles with initial energies of 5.6, 6.1, and 7.8 MeV to ionizing C and F atoms in C_3F_8 ($\rho_l = 1379 \text{ kg m}^{-3}$), shown as a function of the depth of penetration into C_3F_8 [17].

50, 100, and 150 keV energy depositions over $1 \mu\text{m}$ in five separate simulations. The details of the simulation box and energy deposition region geometry are given in [Appendix B](#). The resulting tube of vapor is allowed to evolve in an NPT ensemble with periodic boundary conditions on all sides. This means that each micron-long vapor chunk is evolving exactly as if it was surrounded by the same vapor chunks on both sides, imitating long alpha-particle tracks quite well. We observe that among the tested configurations, only the vapor tube produced as the result of a $10 \frac{\text{keV}}{\mu\text{m}}$ energy deposition is separated into several protobubbles, all of which eventually collapse, as shown in [Fig. 5](#). All other tubes keep expanding irreversibly as in [Fig. 6](#). In [Fig. 7](#), we show the evolution of the vapor tube volumes resulting from $E_{\text{dep}} \geq 30 \text{ keV}$. This observation implies that the three ^{222}Rn chain α particles ([Eq. 7](#)) will predominantly not form protobubbles along their ionization tracks, as the per- μm energy depositions are smaller than 30 keV only over the last few microns to the right of the Bragg peaks (see [Fig. 4](#)).

This leads us to the conclusion that any bubble nucleated as the result of energy deposition by an α particle will evolve similarly to a bubble resulting from a nuclear recoil considered in [Secs. II B](#) and [II C](#). If we further approximate the Bragg curves from [Fig. 4](#) by uniform depositions of E_α (5.6, 6.1, and 7.8 MeV) over the respective penetration depths, the evolution of the produced bubbles will be described, as in the nuclear recoil case, by [Eq. 1](#). The latter will apply at all times when an α -induced bubble may be considered spherical, i.e. $t \geq t_s$, where t_s is to be estimated using [Eq. 5](#) for $l_{\text{cyl}} = 42.6, 48.3$, and $70.0 \mu\text{m}$ (given in the order of increasing E_α). In [Table II](#), we list the estimated times following the instant of the α -induced heat spike at which the resulting bubbles acquire spherical shapes, as well as the corresponding bubble radii.

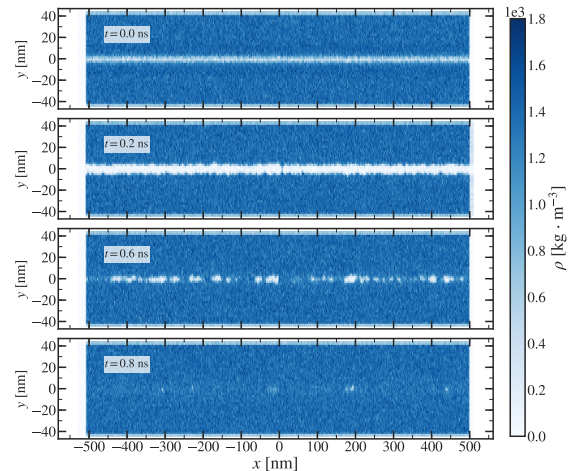


FIG. 5. Example time evolution of a $1 \mu\text{m}$ long vapor region resulting from a 10 keV energy deposition into this region by an α particle. The vapor tube splits into several protobubbles (panel 3), all of which eventually collapse due to insufficient energy deposition. Given α particles from [Fig. 4](#), only small fractions of each α -induced bubble will collapse as shown here, with dominant portions of α tracks getting higher E_{dep} per μm and expanding as in [Fig. 6](#).

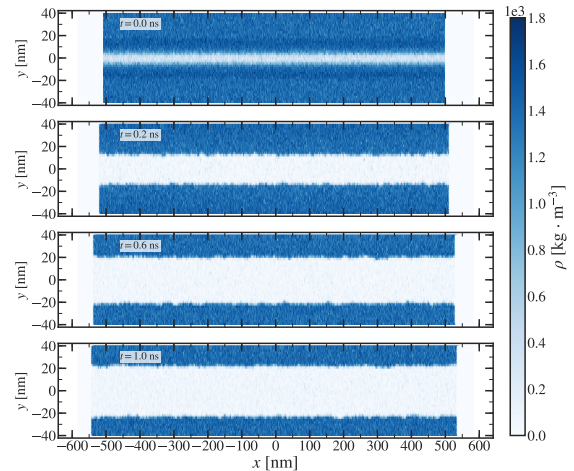


FIG. 6. Example time evolution of a $1 \mu\text{m}$ long vapor region resulting from a 50 keV energy deposition into this region by an alpha-particle. Unlike in [Fig. 5](#), here the vapor tube expands irreversibly, which will be the case for major fractions of α tracks from [Fig. 4](#). The red contours show the boundaries of the vapor tube regions found as in [Sec. II B](#).

E. Extraction of acoustic signal

Using [Eq. 1](#), we modeled the evolution of bubbles nucleated as the result of energy depositions by both nuclear recoils ([Sec. II C](#)) and α particles ([Sec. II D](#)), starting from the time when these bubbles become spherical. Given $R(t)$ in each case, we follow [15] to evaluate the total

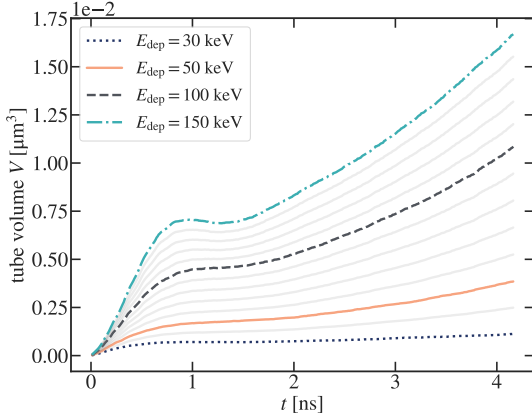


FIG. 7. Evolution of the volumes of μm -long vapor regions imitating parts of alpha-particle tracks for four attempted energy deposition values. The solid gray lines represent the $V(t)$ curves predicted for $E_{\text{dep}} = N \cdot 10 \text{ keV}$, $N \in \mathbb{N}$ by interpolation.

E_{α} [MeV]	l_{cyl} [μm]	R_s [μm]	t_s [μs]
5.6	42.6	16.2 ± 1.2	3.5 ± 0.3
6.1	48.3	18.4 ± 1.4	4.0 ± 0.3
7.8	70.0	26.6 ± 2.1	5.7 ± 0.4

TABLE II. Estimates of the time t_s when α -induced bubbles become spherical and their radii R_s at that moment. The values of t_s and R_s are evaluated with Eqs. 5 and 6 respectively for alphas from the ^{222}Rn decay chain (7). The reported l_{cyl} values correspond to the mean track ranges of α particles in the superheated C_3F_8 ($\rho_1 = 1379 \text{ kg m}^{-3}$), projected with SRIM [17] for each E_{α} .

power radiated in sound waves in all directions:

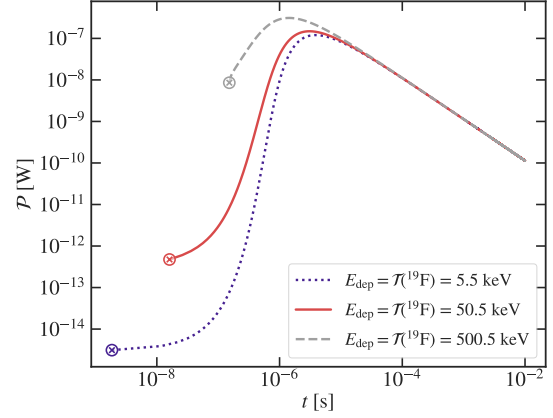
$$\mathcal{P}(t) = \frac{\rho_1 \ddot{V}^2}{4\pi c}, \quad (8)$$

where \ddot{V} is the second time derivative of the bubble volume $V(t) \equiv \frac{4}{3}\pi R^3(t)$ and $c \approx 333 \text{ m s}^{-1}$ is the speed of sound in the liquid phase of superheated C_3F_8 at $T = 14^\circ\text{C}$. In Fig. 8, we plot the acoustic power evaluated from Eq. 8 as a function of time for fluorine recoils with energies $\mathcal{T} = 5.5, 50.5$, and 500.5 keV , with corresponding l_{cyl} extracted from SRIM [17], as well as the three α -induced bubbles from Table II.

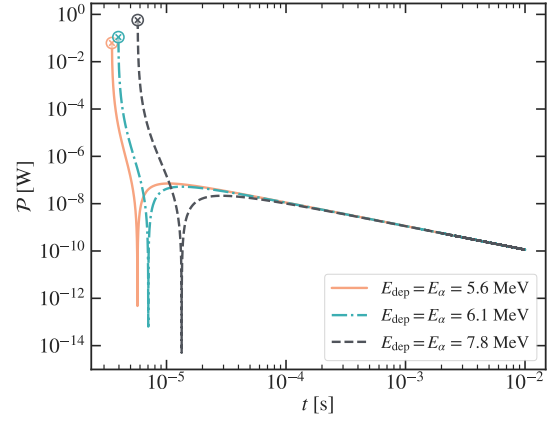
To find the frequency spectrum of the extracted acoustic signal, we compute discrete Fourier transform (DFT) of the time-dependent acoustic pressure:

$$p_{\text{ac}}(t) = \frac{\rho_1 \ddot{V}}{4\pi c}. \quad (9)$$

Fig. 9 gives the resulting frequency spectra for the cases considered in Fig. 8. In this study, we focus on the frequency range of 1–300 kHz to compare our distributions of acoustic energies E_{ac} to those observed in the PICO-60



(a) $\mathcal{P}(t)$ for bubbles nucleated from fluorine recoil-like energy depositions of $\mathcal{T} = 5.5, 50.5$, and 500.5 keV .



(b) $\mathcal{P}(t)$ for bubbles nucleated from α -like energy depositions of $E_{\alpha} = 5.6, 6.1$, and 7.8 MeV over the respective track lengths listed in Table II.

FIG. 8. Acoustic power \mathcal{P} radiated during bubble expansion as a function of time t elapsed after the heat spike. Each $\mathcal{P}(t)$ curve starts at time t_s when the bubble becomes spherical (see Eq. 5), which is marked as a circled cross in each plot. The power is evaluated from the bubble radius evolution at $t \geq t_s$ according to Eq. 8.

calibration runs [2, 4]. Specifically, we evaluate

$$E_{\text{ac}}(1\text{--}300 \text{ kHz}) \equiv \int_{1 \text{ kHz}}^{300 \text{ kHz}} |\mathcal{A}(f)|^2 \text{ d}f, \quad (10)$$

with $\mathcal{A}(f)$ being the complex amplitude of the DFT at a frequency f in the returned samples and $|\mathcal{A}(f)|^2$ giving the respective power spectrum.

From Fig. 8a, we see that at times $t \geq t_s$, only a short interval covers $\mathcal{P}(t)$ monotonically increasing with t for nuclear recoil events. Near $t \sim 1 \mu\text{s}$, a maximum in $\mathcal{P}(t)$ is observed, after which the bubble growth slows down in the thermal phase and $\mathcal{P}(t)$ starts to drop. In Fig. 8b, we find a similar pattern in the acoustic power radiation due to expansion of α -induced bubbles. A sudden drop in $\mathcal{P}(t)$

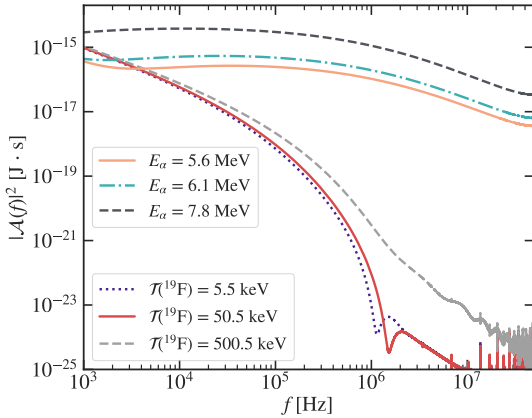


FIG. 9. Frequency spectra of the acoustic power radiated during expansion of nuclear recoil and α -induced bubbles. The amplitudes were computed via discrete Fourier transform of the time-dependent pressure signal (9).

indicates an inflection point characteristic of the times close to t_s . At all times prior to t_s , the bubbles are not yet spherical and hence the exact $R(t)$ behavior cannot be predicted with the current model. However, using the $R(t)$ data obtained directly from LAMMPS simulations, we found that $\mathcal{P}(t)$ at $t \leq t_s$ is nearly six orders of magnitude smaller than $\mathcal{P}(t)$ at $t \geq t_s$ in the 1–300 kHz frequency range, which lets us neglect the contribution from the former.

III. GENERATION OF ACOUSTIC PARAMETER DISTRIBUTION

In the PICO experiment, a typical data analysis reports the distribution of AP (acoustic parameter) values. The latter are derived directly from the magnitude of the acoustic signal recorded during the expansion of all bubbles observed as single events in the fiducial volume during the run. Neutron-induced nuclear recoils form a low-AP peak in the AP distribution. Expansion of α -induced bubbles, which are background events in both calibration and dark matter search runs, is accompanied by radiation of larger acoustic energies. Accordingly, α events feature AP values higher than those characteristic of nuclear recoil (NR) events, and form distinguishable peaks to the right of the latter. The collected data are typically normalized so that center of the NR peak has an AP value of 1.

In Sec. II E, we described a general technique for evaluating the acoustic energy E_{ac} emitted in 1–300 kHz frequency range for both nuclear recoil and α -like energy depositions. Additionally, we provided specific examples of E_{ac} calculation for fluorine recoil energies $\mathcal{T} \in \{5.5, 50.5, 500.5\}$ keV and alpha energies $E_\alpha \in \{5.6, 6.1, 7.8\}$ MeV. For all cases, a uniform energy deposition along the SRIM-derived mean ranges of F/He

ions in C_3F_8 was assumed. In reality, however, each projected track length value is subject to certain variation $\sigma(l_{\text{cyl}})$ due to collisions, which can be extracted from SRIM as longitudinal straggling [17]. This variation will inevitably translate into a spread in times t_s when the nucleated bubbles become spherical, as well as their radii $R_s = R(t_s)$, according to Eqs. 5 and 6. Ultimately, we will obtain a distribution of radiated acoustic energies that will reflect the variations in the length of the energy deposition region l_{cyl} .

For the nuclear recoil energies \mathcal{T} , we consider a range from 0.5 to 1000.5 keV with a step of $\Delta\mathcal{T} = 5$ keV. Taking into account recoil energies exceeding 1 MeV will not contribute much to the resulting distribution of acoustic energies, for the probability of such high \mathcal{T} is very small. To prove this, we invoke the kinematics of $^{241}\text{Am}/^9\text{Be}$ source neutrons, whose original spectra were measured in e.g. [18] with high precision. These neutrons enter the detector from the outside and propagate through the hydraulic fluid on their way to the target C_3F_8 . By simulating this propagation in Geant4 [19] with the geometry of the PICO-40L detector, we obtain a shifted spectrum of $^{241}\text{Am}/^9\text{Be}$ neutrons, now directly incident on the target nuclei. For an arbitrarily normalized fluence, this spectrum is shown in Fig. F.2. We note that an $^{241}\text{Am}/^9\text{Be}$ source spectrum closely resembles that of a ^{252}Cf source, which is why we omit a separate discussion of ^{252}Cf neutron kinematics. Convolution of this spectrum with the cross sections of elastic neutron-nucleus scattering [20] gives the distribution of the normalized probabilities of carbon and fluorine recoils shown in Fig. 10. We see that recoil energies above 1 MeV are less probable than the energies up to 100 keV by nearly 2 orders of magnitude, justifying our choice of the recoil energy range.

To generate an AP distribution resembling that obtained experimentally, we consider a sample of 11,000 neutron-induced recoils (among which 3,000 are those of ^{12}C and 8000 are those of ^{19}F) and 5,000 energy depositions by each of the α particle types (7). The NR sample will have a well-defined continuous distribution of energies following Eq. E4. Each of these energies corresponds to a certain range l_{cyl} of a C/F ion, which we show in Fig. F.1, and an associated longitudinal straggling $\sigma(l_{\text{cyl}})$. Thus, given N_i samples in the recoil energy range $[\mathcal{T}_i, \mathcal{T}_i + \Delta\mathcal{T}]$, we can generate a Gaussian distribution of carbon and fluorine ion ranges centered at the mean values extracted from SRIM and having $\sigma(l_{\text{cyl}})$ as a standard deviation. The size of that distribution will also be equal to N_i . This results in the respective distribution of energy depositions per unit length, $\frac{E_{\text{dep}}}{l_{\text{cyl}}}$, where E_{dep} is now equal to \mathcal{T}_i . Eqs. 5 and 6 are then used to predict the time t_s when the nucleated bubbles will become spherical and their radii R_s at that point. From here, each NR instance in the distribution will have an associated bubble growth curve $R(t)$ generated from Eq. 1. In turn, $R(t)$ gives the acoustic power $\mathcal{P}(t)$ radiated at $t \geq t_s$ (see Eq. 8). The acoustic pressure signal (9) is then Fourier-transformed, and its normalized power spectrum is integrated over

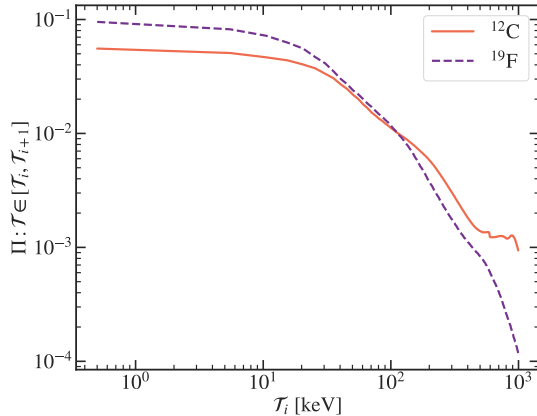


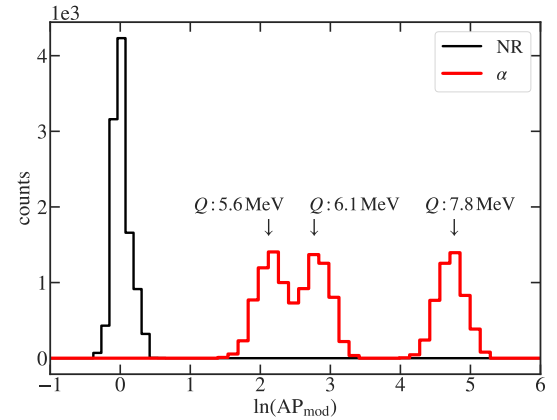
FIG. 10. Normalized probabilities of C/F recoils having the energy between T_i and $T_{i+1} = T_i + \Delta T$ ($\Delta T = 5$ keV) as the result of elastic scattering of $^{241}\text{Am}/^9\text{Be}$ source neutrons (the spectrum shown in Fig. F.2). For a neutron entering the C_3F_8 medium, the shown probability curves will be suppressed by factors of 3/11 and 8/11 for C and F nuclei respectively, which we take into account by generating 3,000 carbon recoil-like samples and 8,000 fluorine recoil-like samples when modeling the distributions of radiated acoustic energies.

the frequency range of 1–300 kHz to obtain the acoustic energy E_{ac} emitted at $t \geq t_s$ up to 0.01 s. In this way, for each recoil energy T_i of carbon and fluorine ions, we are able to evaluate the acoustic energy emission at all stages of bubble growth following t_s . This part of the calculation results in the low- E_{ac} nuclear recoil peak in the modeled distribution. The procedure of generating the distribution of acoustic energies radiated during expansion of the α -induced bubbles is effectively identical, except only three populations of deposited energies are possible, which we assume to be equally probable.

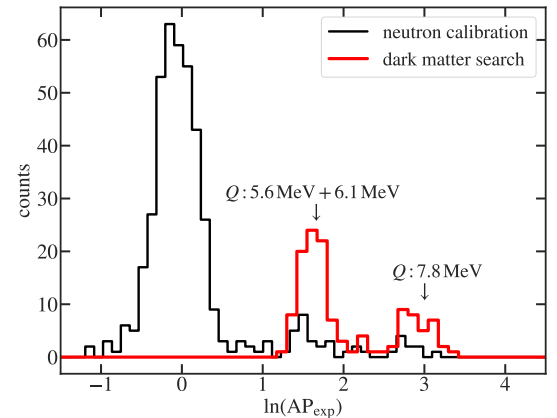
Sec. IV presents the distribution of acoustic energies radiated by neutron-induced and α -induced bubbles in a PICO-like bubble chamber. The uncertainties on E_{ac} values that are derived from the uncertainties on the model parameters (A, B, γ, ν_1, R_s , and t_s) are not taken account in generating such a distribution, as it would only result in a global shift of all AP values.

IV. RESULTS AND DISCUSSION

Following renormalization of the simulated acoustic energies by the Gaussian mean of those radiated in nuclear recoil-induced bubble expansions, we obtain the distribution of AP values shown in Fig. 11a. We immediately observe that the derived AP pattern provides perfect discrimination between neutron-induced nuclear recoils and α particles in 1–300 kHz frequency range. It can therefore be directly compared to the experimental AP distribution from the PICO-60 run [2, 3] with 52 kg of C_3F_8 , which we reproduce in Fig. 11b.



(a) Distribution of the modeled AP values for bubbles nucleated by neutron-induced C/F recoils and the three ^{222}Rn decay chain α -particle populations (7). The data is normalized so that the Gaussian center of the NR peak has an AP_{mod} value of 1. The procedure followed to arrive at the AP_{mod} distribution is described in Sec. III.



(b) AP distribution as obtained from the PICO-60 run at temperature $T_0 = 13.9^\circ\text{C}$ and pressure $P_1 = 30.2$ psia (208 kPa), corresponding to the bubble nucleation energy threshold of 3.3 keV [2, 3]. Both $^{241}\text{Am}/^9\text{Be}$ and ^{252}Cf sources were used for neutron calibration.

FIG. 11. Comparison of the modeled and the experimental acoustic parameter (AP) distributions. “NR” stands for the population of bubbles induced by nuclear recoils, which occur due to elastic scattering of calibration neutrons. The rest of the presented data, which appears under the label “ α ,” is the population of bubbles nucleated by α particles from the $^{222}\text{Rn} \rightarrow ^{210}\text{Pb}$ decay chain (7). Q -values of the respective decays are listed above each α peak. In deriving AP_{mod} , we assumed energy depositions by the alphas to be equal to these Q -values.

Comparing the modeled and the experimentally obtained AP patterns, we report good qualitative agreement between the two, with larger AP values being a characteristic signature of α particle-induced bubbles in both cases. This outcome confirms that the spherical bubble growth model (1) is a plausible description of bubble dynamics for

both NR- and α -induced bubbles, as it correctly predicts the relative magnitudes of acoustic signals associated with the two bubble nucleation scenarios. The AP-based α particle discrimination used by the PICO collaboration thereby becomes fully motivated by a physical model for the first time.

Quantitatively, we find differences between the modeled and the simulated AP in both the means of the NR/alpha peaks and the spread of AP values about these means. The discrepancies between the exact positions of the corresponding peaks on Figs. 11a and 11b are not surprising. Indeed, in this study, we evaluated acoustic energy emitted in all directions during bubble expansion and converted it to AP_{mod} directly. In the experimental data, AP_{exp} is a measure of the acoustic signal magnitude as recorded by the piezoelectric sensors, the response of which is dependent not only on the total energy radiated in sound waves, but also on the exact sound wave propagation characteristics and the accompanying chamber wall vibrations. Several simplifications have been made prior to arriving at the acoustic emission model as well, such as describing C_3F_8 as a LJ fluid at the stage of molecular dynamics simulations. We therefore do not expect the AP_{mod} values to match the AP_{exp} ones exactly. The question of intrinsically higher NR peak resolution and clearer separation of the 5.6 MeV and 6.1 MeV alpha peaks is of a similar nature. In our model, only the energies being deposited and the statistical variation in the respective ion ranges give rise to a continuum of radiated acoustic energies. In a more realistic scenario, the presence of noise in the recorded signal, limited transducer sensitivity, and the precision of bubble position reconstruction all contribute to the width of each observed peak, along with the aforementioned physical reasons. A full treatment of sound wave propagation in the PICO bubble chambers and instrumental responses to the original acoustic signal would be required to predict the exact smearing effects on the peaks from Fig. 11a. Such a study falls beyond the scope of the present work and is in progress within the PICO collaboration.

V. CONCLUSIONS

In this paper, we attempted to physically motivate acoustic α -particle background discrimination in C_3F_8 -filled PICO bubble chambers. The model that we have constructed builds on predictions for bubble growth dynamics, depending heavily on initial conditions set by nuclear recoil and alpha ionization but otherwise described by exactly the same physics in the two cases. It has been previously thought that the μm -scale α ranges in C_3F_8 result in the formation of multiple protobubbles along each track, which was the working explanation for the large observed acoustic signal magnitude [2, 4, 5, 9]. We have shown in Sec. IID that the MeV-scale energies brought into C_3F_8 by $^{222}\text{Rn} \rightarrow ^{210}\text{Pb}$ chain α particles inevitably result in the nucleation of only a single bubble for each α

track. This has given us the grounds to apply a universal approach in evaluating the acoustic energies radiated during bubble expansion by both α -induced and nuclear recoil-induced bubbles, based on the volume change rate of a single bubble, as per [15]. With this simple idea, we were able to reproduce the main empirical finding of [2]; namely, the stronger acoustic signature of all α events relative to the nuclear recoils. A successful reconstruction of such a pattern serves as a credibility check for the proposed bubble growth and acoustic emission model, applicable to both types of ionizing radiation considered.

To arrive at the aforementioned conclusions, we have employed several major simplifications. First, we developed a Lennard-Jones potential formulation of the intermolecular forces in superheated C_3F_8 by conducting a set of thermodynamic experiments within the LAMMPS framework for molecular dynamics [8]. This allowed us to simulate bubble nucleations in a simple system of atomic complexity, which behaves like C_3F_8 with the exception of $\lesssim 30\%$ deviations of equilibrium pressure, surface tension, and vapor density at saturation from their measured values [11]. Then, with the aid of molecular dynamics simulations, we studied how the length of the energy deposition region and the energy being deposited impact the time when the nucleated bubble becomes spherical, the size of the bubble at that moment, and the acoustic energy emitted prior to it. Sec. IIE gives the relations derived from a set of simulations, all continuing up to several nanoseconds after the heat spike. We note that in all simulations the ionizing energy was deposited uniformly along cylindrical regions of arbitrarily chosen small radius. This is a first-order approximation to the actual functional dependencies of the energy depositions per unit length on the depth of penetration of an ionizing particle into the target medium. Another simplification that we introduced is that of each alpha depositing the full energy released in the respective decay from Eq. 7. This means that we disregarded bubble nucleations by recoils of heavy nuclei (^{218}Po , ^{214}Po , and ^{210}Pb), as we assumed the alphas to take over and deposit all of the released energy. Given the fact that both α -induced and nuclear recoil-induced bubbles eventually acquire spherical shapes, we used the findings of Sec. IIE and the well-known spherical bubble growth model (1) to predict the evolution of any bubble at times not accessible to molecular dynamics simulations due to computational costs. Finally, using a realistic sample of carbon and fluorine recoil energies in addition to the three discrete α particle energies, we obtained a distribution of acoustic energies closely resembling that obtained in the PICO-60 experiment. The simulated data exhibits much higher resolution of both nuclear recoil and alpha peaks compared to the experimental results (see Sec. IV), which we attribute to acoustic detector effects not taken into account in this study. These differences aside, we come to the first model-based discrimination of α background from calibration neutron-induced nuclear recoils, which have kinematics similar to that of WIMPs. This justifies the approach currently used in all PICO

analyses to distinguish the WIMP candidate signal from the α background.

The present study can be further expanded by considering other types of background radiation relevant to underground bubble chambers. In particular, bubble nucleation by electron recoils has been of continued interest. The PICO collaboration has recently discovered that the Seitz model [12] for bubble nucleation at moderate superheats only applies to nuclear recoils and alpha interactions [21]. Electron recoils, due to the extraordinary suppression at the thermodynamic operation point of dark matter bubble chambers, follow a different model of threshold behavior than that predicted by the Seitz model. Therefore a separate set of molecular dynamics simulations would be required to investigate how the electron recoil bubble nucleation mechanism influences the timeline and magnitude of acoustic emission.

VI. ACKNOWLEDGEMENTS

We wish to acknowledge an earlier study on molecular dynamics simulations of bubble nucleation in direct dark matter search detectors by Denzel et al. [9], which formed the foundation of the present work. In particular, we thank Philipp Denzel for useful clarifications on their publication and making the developed code publicly available via phdenzel.github.io. The computational resources and support were kindly provided by Compute Canada (www.computecanada.ca), SciNet, and WestGrid. We thank Gabriel Hanna, Bruce Sutherland, and John Beamish of the University of Alberta for helpful discussions on components of this study. We also wish to acknowledge the support of the Natural Sciences and Engineering Research Council of Canada (NSERC) for funding.

[1] D. A. Glaser and D. C. Rahm, *Phys. Rev.* **97**, 474 (1955).

[2] C. Amole et al. (PICO Collaboration), *Phys. Rev. Lett.* **118**, 251301 (2017).

[3] C. Amole et al. (PICO Collaboration), arXiv:1902.04031 [astro-ph.CO] (2019).

[4] P. Mitra, Ph.D. thesis, University of Alberta (2018).

[5] F. Aubin, M. Auger, M.-H. Genest, G. Giroux, R. Gornea, R. Faust, C. Leroy, L. Lessard, J.-P. Martin, T. Morlat, et al., *New J. Phys.* **10**, 103017 (2008).

[6] M. S. Plesset and S. A. Zwick, *J. Appl. Phys.* **25**, 493 (1954).

[7] L. Rayleigh, *Lond. Edinb. Dubl. Phil. Mag.* **34**, 94 (1917).

[8] S. Plimpton, *J. Comput. Phys.* **117**, 1 (1995).

[9] P. Denzel, J. Diemand, and R. Anglil, *Phys. Rev. E* **93** (2016).

[10] M. Felizardo et al. (SIMPLE Collaboration), *Physical Review Letters* **108**, 201302 (2012).

[11] E. W. Lemmon, I. Bell, M. L. Huber, and M. O. McLinden, *NIST Standard Reference Database 23: Reference Fluid Thermodynamic and Transport Properties-REFPROP, Version 10.0, National Institute of Standards and Technology* (2018).

[12] F. Seitz, *Phys. Fluids* **1**, 2 (1958).

[13] W. E. Lorensen, H. E. Cline, W. E. Lorensen, and H. E. Cline, *ACM SIGGRAPH Computer Graphics* **21**, 163 (1987).

[14] S. v. d. Walt, J. L. Schnberger, J. Nunez-Iglesias, F. Boulogne, J. D. Warner, N. Yager, E. Gouillart, and T. Yu, *PeerJ* **2**, e453 (2014).

[15] L. Landau and E. Lifshitz, *Fluid Mechanics*, v. 6 (Elsevier Science, 2013).

[16] B. B. Mikic, W. M. Rohsenow, and P. Griffith, *Int. J. Heat Mass Transf.* **13**, 657 (1970).

[17] J. F. Ziegler, M. D. Ziegler, and J. P. Biersack, *Nucl. Instrum. Meth. Phys. Res. B* **268**, 1818 (2010).

[18] J. Marsh, D. Thomas, and M. Burke, *Nucl. Instrum. Meth. Phys. Res. A* **366**, 340 (1995).

[19] S. Agostinelli, J. Allison, K. Amako, J. Apostolakis, H. Araujo, P. Arce, M. Asai, D. Axen, S. Banerjee, G. Barraud, et al., *Nucl. Instrum. Meth. Phys. Res. A* **506**, 250 (2003).

[20] D. A. Brown, M. B. Chadwick, R. Capote, A. C. Kahler, A. Trkov, M. W. Herman, A. A. Sonzogni, Y. Danon, A. D. Carlson, M. Dunn, et al., *Nucl. Data Sheets* **148**, 1 (2018).

[21] C. Amole et al. (PICO Collaboration), arXiv:1905.12522 [physics.ins-det] (2019).

[22] J. E. Jones, *Proc. R. Soc. Lond. A* **106**, 463 (1924).

[23] S. Toxvaerd and J. C. Dyre, *J. Chem. Phys.* **134**, 081102 (2011).

[24] J. Diemand, R. Anglil, K. K. Tanaka, and H. Tanaka, *Phys. Rev. E* **90** (2014).

[25] J. P. R. B. Walton, D. J. Tildesley, J. S. Rowlinson, and J. R. Henderson, *Mol. Phys.* **48**, 1357 (1983).

[26] G. A. Chapela, G. Saville, S. M. Thompson, and J. S. Rowlinson, *J. Chem. Soc. Faraday Trans. 2* **73**, 1133 (1977).

[27] J. G. Kirkwood and F. P. Buff, *J. Chem. Phys.* **17**, 338 (1949).

[28] S. Cheng, J. B. Lechman, S. J. Plimpton, and G. S. Grest, *J. Chem. Phys.* **134**, 224704 (2011).

[29] B. R. Novak, E. J. Maginn, and M. J. McCready, *Phys. Rev. B* **75**, 085413 (2007).

[30] M. A. González, G. Menzl, J. L. Aragones, P. Geiger, F. Caupin, J. L. F. Abascal, C. Dellago, and C. Valeriani, *J. Chem. Phys.* **141**, 18C511 (2014).

[31] M. A. González, J. L. F. Abascal, C. Valeriani, and F. Bresme, *J. Chem. Phys.* **142**, 154903 (2015).

Appendix A: Lennard-Jones potential parameters for C_3F_8

In molecular dynamics simulations, the Lennard-Jones (LJ) potential [22] is a common way to describe simple interatomic interactions pair-by-pair. Changing with distance r between the atoms as

$$u_{\text{LJ}}(r) = 4\epsilon \left[\left(\frac{\sigma}{r} \right)^{12} - \left(\frac{\sigma}{r} \right)^6 \right], \quad (\text{A1})$$

the LJ potential is defined through the characteristic energy (potential well depth) ϵ and the characteristic length (effective atomic diameter) σ , which are the units used within MD simulations. The potential (A1) is typically cut off at a certain critical distance to reduce computational costs of a simulation. To minimize the error of such a truncation, the interaction force is shifted so that it goes to zero continuously, resulting in a truncated shifted-force Lennard-Jones (TSF-LJ) potential [23]. Following [9, 24], we choose the cutoff radius to be 2.5σ , which ensures the deviation from the full-tail $u_{\text{LJ}}(r)$ to be smaller than 1.6% [23].

Since we aim to compare the results of the present study with the acoustic data from the PICO-60 run at $\sim 14^\circ\text{C}$ [2], it is important to reproduce the major thermodynamic properties of C_3F_8 at this particular temperature, corresponding to $T_0 = 0.778\epsilon/k_{\text{B}}$ in LJ units. For that reason, we repeated the liquid-vapor interface experiment of [24] for $0.778\epsilon/k_{\text{B}}$ to extract equilibrium pressure P_{eq} , liquid/vapor density ρ_l/ρ_v , and surface tension γ in LJ units ($\epsilon\sigma^{-3}$, $m\sigma^{-3}$, and $\epsilon\sigma^{-2}$ respectively, where $m = 188.02\text{ u}$ for C_3F_8) at saturation. We then used the corresponding real values of these quantities from the REFPROP database [11] to deduce the suitable value of σ , with ϵ fixed at 0.0318 eV as discussed in Sec. II A. We started the experiment by creating a simulation box with length and width $L_x = L_y = 200\sigma$ and height $L_z = 100\sigma$, to which we applied periodic boundary conditions, and placing a liquid slab in the middle of the box. The slab initially contained 1,240,000 “atoms” on a lattice, taking the whole XY -plane of the simulation box and 30σ in z direction. The atoms were assigned Maxwell-distributed velocities corresponding to T_0 . To preliminarily randomize their positions, we performed a microcanonical (NVE : constant particle number, volume, and energy) ensemble simulation for 100,000 time steps. A single time step was set equal to 0.0025τ , where $\tau = \sigma\sqrt{m/\epsilon} \approx 4.172\text{ ps}$. In each run, we used a Langevin thermostat to control the temperature. After we obtained such stable liquid conditions, we allowed the system to evolve for 2,000,000 time steps as an NVT (constant particle number, volume, and temperature) ensemble. The purpose of the first 1,000,000 time steps was to obtain two well-equilibrated liquid-vapor interfaces, below and above the liquid slab, after which we were able to take the measurements P_{eq} and ρ_l/ρ_v in the subsequent 1,000,000 time steps. The time averaging of these quantities was performed 20 times in 50,000-time-step-long intervals, which ultimately gave

the 1σ scatter for the global weighted average [24]. The equilibrium pressure was evaluated as the spatial average of the normal (z) component of the pressure tensor [25]. To obtain values for liquid and vapor densities, we produced a density profile of the system over the z -axis, with $\rho(z)$ spatially averaged over chunks of 0.5σ height. The hyperbolic tangent function [26] was then used to fit the time-averaged $\rho(z)$ dependence:

$$\rho(z) = \frac{1}{2}(\rho_l + \rho_v) - \frac{1}{2}(\rho_l - \rho_v) \tanh \left[\frac{2(|z| - z_0)}{d} \right], \quad (\text{A2})$$

where $z = z_0$ defines the plane of the Gibbs dividing surface ($\rho(z_0) = \frac{1}{2}[\rho_l + \rho_v]$) and d is a measure of the interface thickness. The measured density profile and the best-fitting curve of the form (A2) are given in Fig. A.1 along with the temperature distribution in the simulation box.

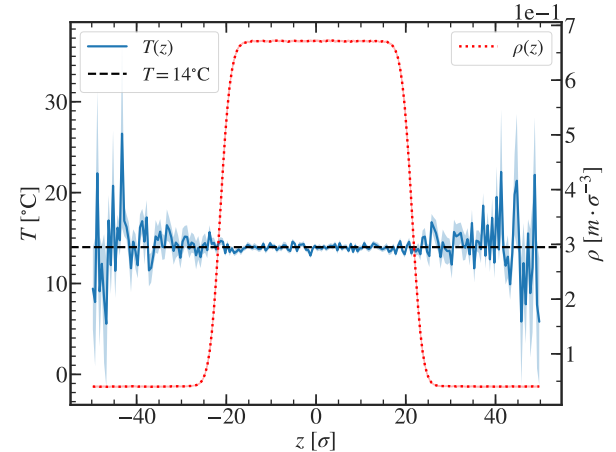


FIG. A.1. Density and temperature profiles in the liquid slab experiment. The temperature $T(z)$ is already converted from the reduced LJ units to $^\circ\text{C}$ using $\epsilon = 0.0318\text{ eV}$, whereas the density $\rho(z)$ is given in units of $m\sigma^{-3}$ and later used as one of the ways to estimate σ (see Table III, rows 2 and 3). The shaded areas correspond to one standard deviation uncertainties on the plotted values.

To compute surface tensions, we followed the Kirkwood-Buff approach [27]:

$$\gamma = \frac{L_z}{2} \left[P_z - \frac{P_x + P_y}{2} \right], \quad (\text{A3})$$

where P_x , P_y , and P_z are the spatially averaged pressures in each direction [28]. Table III presents the results of the P_{eq} , ρ_v , ρ_l , and γ measurements in LJ units; also listed are the respective real values of these quantities extracted from REFPROP database [11] in SI units. We observe that there is not a single value of σ that would reconcile all of the measurements simultaneously. As discussed in Sec. II A, we pick $\sigma \approx 0.533\text{ nm}$ to approximate “intermolecular” interactions within C_3F_8 with the

	MD simulation	REFPROP	σ [nm]
γ	$0.201 \pm 0.001 \frac{\epsilon}{\sigma^2}$	$4.82 \pm 0.05 \frac{\text{mN}}{\text{m}}$	0.461 ± 0.003
ρ_l	$0.6715 \pm 0.0001 \frac{\text{m}}{\sigma^3}$	$1385.1 \pm 0.3 \frac{\text{kg}}{\text{m}^3}$	0.53293 ± 0.00005
ρ_v	$0.03983 \pm 0.00009 \frac{\text{m}}{\sigma^3}$	$62 \pm 1 \frac{\text{kg}}{\text{m}^3}$	0.586 ± 0.003
P_{eq}	$0.02240 \pm 0.00003 \frac{\epsilon}{\sigma^3}$	$6.5 \pm 0.1 \text{ bar}$	0.560 ± 0.003

TABLE III. Liquid slab experiment results: MD measurements of surface tension and liquid/vapor densities at saturation ($T = 14^\circ\text{C}$) in LJ units as compared to REFPROP values in SI units. For each quantity, the last column shows σ that makes the measured LJ value match the REFPROP-predicted value. The uncertainties on REFPROP values are derived from the uncertainties on simulation-extracted temperatures for each phase ($T_l = 13.95 \pm 0.05^\circ\text{C}$, $T_v = 14.4 \pm 0.5^\circ\text{C}$); see Fig. A.1.

Lennard-Jones potential. This matches the simulation extracted liquid density at 14°C with the corresponding REFPROP value and introduces $\lesssim 30\%$ errors on other quantities listed in Table III.

Appendix B: Heat spike simulation procedure

For the bubble nucleation simulation, we chose a cubic box extending from $-\frac{L_i}{2}$ to $\frac{L_i}{2}$ in each dimension ($i = \bar{x}, \bar{y}, \bar{z}$), with $L_i \approx 363.2\sigma$. This box was then filled with 32,000,000 atoms on a face-centered cubic lattice, corresponding to $\rho_l = 0.668 \frac{\text{m}}{\sigma^3}$. As per Appendix A, the latter value was chosen so as to reproduce the density of superheated C_3F_8 at $T_0 = 14^\circ\text{C}$, $P_l = 207 \text{ kPa}$, which is equal to $1379 \frac{\text{kg}}{\text{m}^3}$ [11]. Periodic boundary conditions were applied in all three directions. Following the approach of [9] to bring an LJ fluid to a superheated metastable state, we started our system at a temperature exceeding T_0 , namely $0.8 \epsilon/k_B$ (22°C). Together with the chosen ρ_l , this gave us stable liquid conditions, which were retained for 10,000 time steps in an *NVE* ensemble to equilibrate the system. The temperature was fixed throughout this preliminary equilibration. The next step was to linearly lower the temperature from $0.8 \epsilon/k_B$ to the target $0.778 \epsilon/k_B$ over the time interval of 15,000 steps, which was again done in an *NVE* ensemble. Since the system volume – and hence, the liquid density – was kept fixed throughout the procedure, we ended up having a density that was now too low for $0.778 \epsilon/k_B$, as it should have been increased proportionally to account for the decrease in T and maintain the system in a stable liquid state. Thus, the liquid became superheated. To equilibrate the system at these new conditions, it was evolved for another 30,000 time steps under *NVE* constraints, with temperature fixed for the first 15,000 steps and freed until the end of this procedure.

Following the instant of a sufficiently energetic heat spike in the prepared superheated fluid, the approach of Denzel et al. in [9] was to integrate the system in an *NVE* ensemble until the pressure in the liquid would increase

significantly. This effect was explained by the continuing bubble growth in a tiny volume ($[323.6\sigma]^3 \approx [162 \text{ nm}]^3$), which would further slow down unrealistically because of the rising pressure. Although our simulation volume was slightly larger ($[363.2\sigma]^3 \approx [194 \text{ nm}]^3$), this issue could not have been easily prevented, as we aimed to simulate much larger bubbles (for comparison, $R_c = 10.47\sigma \approx 5.3 \text{ nm}$ in [9]), potentially affecting the pressure in a fixed-volume ensemble even more. One way to avoid this complication would be to simulate a liquid volume so big that the bubble expansion would have almost no influence on the overall liquid pressure. This solution, however, comes at the expense of increased simulation time and respective demand for computational resources. A major fraction of the latter would be spent on integrating the equations of motion for the liquid phase of the system far away from the bubble, which is of no interest for this or any other study in which nucleation and evolution of a single bubble is the central topic. Therefore, we chose to avoid simulation volume scaling and deviate from the method described in [9] by switching from an *NVE* to an *NPT* ensemble for the post-spike part of the simulation. In *NPT* integration, the overall particle number, pressure, and temperature are preserved, solving the rising pressure problem by default and reproducing typical bubble chamber conditions (P_l, T kept constant). Other cases where an *NPT* ensemble was chosen to govern bubble evolution in superheated fluids are reported in, for example, [29–31].

For α -induced bubble nucleation simulations, we set up a simulation box with $L_x = 1888.6\sigma \approx 1 \mu\text{m}$ and $L_z = L_y = 159.8\sigma \approx 85 \text{ nm}$ in LAMMPS. As before, we required $\rho_l = 0.668 \text{ m} \sigma^{-3} = 1379 \text{ kg m}^{-3}$ and $T = 0.778 \epsilon/k_B = 14^\circ\text{C}$. To superheat the liquid, we followed the same procedure as in the nuclear recoil case. However, several modifications to the energy deposition region geometry were made. We observed that if the cylinder radius r_{cyl} was set to 2σ as in the nuclear recoil simulation, the *NPT* integrators failed to maintain the requested $0.778 \epsilon/k_B$ temperature for the whole system due to overly high temperature within the cylinder. To overcome this issue, we enlarged the radius to 3σ . The cylinder length was set equal to the simulation box length $L_x = 1 \mu\text{m}$ for easier comparison with the per- μm energy depositions given in Fig. 4.

Appendix C: Bubble surface tracking

Throughout the MD simulations in LAMMPS, we made use of a grid of cubic cells of size $[4\sigma]^3$ and computed the numbers of atoms falling within these cells as averaged over 1000 time steps ($\approx 0.01 \text{ ns}$) intervals. After each such interval, we saved a slice of the resulting spatial density distributions into a text file. With the energy deposition axis parallel to the x -axis and centered at $y = 0, z = 0$, we took the slice between $-2\sigma \leq z \leq 2\sigma$. This allowed us to record the 2D evolution of the post-spike densities in the XY plane.

After that, we applied the `measure.find_contours` function of the `scikit-image` Python module [13, 14] to extract the bubble contour at each moment in time. This function acts upon the density data structured as a 2D array and returns discrete sets of points x_i, y_i for all the contours where $\rho_l(x_i, y_i) = c$ holds. With a suitable choice of c , one of the contours found with this method will be that of the vapor-liquid boundary – that is, the contour of the bubble slice at $z = 0$. Our tests showed that choosing the longest contour among those extracted is a perfectly robust method to pick up the bubble “surface” boundary if we require $c = 0.4 \text{ m} \sigma^{-3} \approx 830 \text{ kg m}^{-3}$.

This method of bubble surface tracking was developed as an alternative to recursive linking of vapor cells used in [9, 24], for two main reasons. First, in this study we are only interested in the evolution of a single bubble. Identification of vapor regions in the rest of the liquid volume (originally introduced in [24] for the case of homogeneous nucleation) would be a redundant procedure here, requiring information about randomly distributed and negligibly small vapor cells to be stored in memory. In our approach, only the longest contour from the set of `measure.find_contours` outputs is saved at each t , while all other variables are overwritten as soon as the algorithm goes to the next “frame.”

Appendix D: Transition from nonspherical to spherical bubble shape and further dynamics

The differential form of Eq. 1 is universal for all spherical bubbles irrespective of how they were nucleated. Parameters A, B, γ , and ν_l in Eq. 1 are also shared between the different bubble expansions in the same liquid. We may therefore fit a few of the simulated bubble growth histories $R(t)$ for these parameters and use the best-fitting values later on to predict the dynamics of any bubble expanding within our LJ fluid. For this purpose, we use the bubble evolution data from four simulations mimicking energy depositions by nuclear recoils. These include $E_{\text{dep}} = 5 \text{ keV}$ deposited along $2R_c$; $E_{\text{dep}} = 5 \text{ keV}$ along $4R_c$; $E_{\text{dep}} = 3.75 \text{ keV}$ along $2R_c$; and $E_{\text{dep}} = 2.5 \text{ keV}$ along $2R_c$. We restrict the fit to those parts of the data where the bubbles are already spherical (red crosses in Fig. D.1). To avoid overfitting, we find it advantageous to fix A at 17.7 m s^{-1} , which is the value we predict from Eq. 2 and Table I for C_3F_8 . We let B, γ , and ν_l be free parameters that are shared between the four data sets we described, and arrive at the results in Table I.

While these parameters are universal for any bubble nucleated within the LJ fluid, the initial conditions for the spherical bubble growth equation (1) vary with deposited energy and ion track length. This is reflected in Figs. D.2 and D.3. The time t_s of transition to bubble sphericity has an apparent dependence only on the length of the energy deposition region. The bubble radius R_s at t_s is also affected by the energy deposited. We combine these observations in Eqs. 5 and 6.

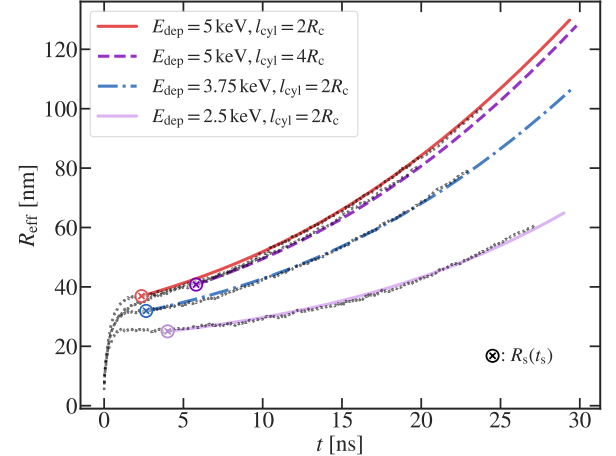


FIG. D.1. The results of simultaneous fitting of the numerical solution to Eq. 1 to the bubble growth curves obtained from four LAMMPS simulations of bubble nucleation. The cross-shaped markers represent the times when the bubbles become spherical and their respective sizes. These are the starting points of the data portions to be fitted, acting as initial conditions for Eq. 1 and found as described in Fig. 2b.

Appendix E: Probabilities of nuclear recoil energies

Each incident neutron energy E_n allows for a continuum of nuclear recoil energies \mathcal{T} and scattered neutron energies E'_n , such that $E'_n = E_n - \mathcal{T}$. The probability density ξ at the recoil energy \mathcal{T} follows

$$\xi(E_n, \mathcal{T}) = \begin{cases} \frac{1}{(1-\beta)E_n}, & \text{if } \beta E_n \leq E_n - \mathcal{T} \leq E_n; \\ 0 & \text{otherwise,} \end{cases} \quad (\text{E1})$$

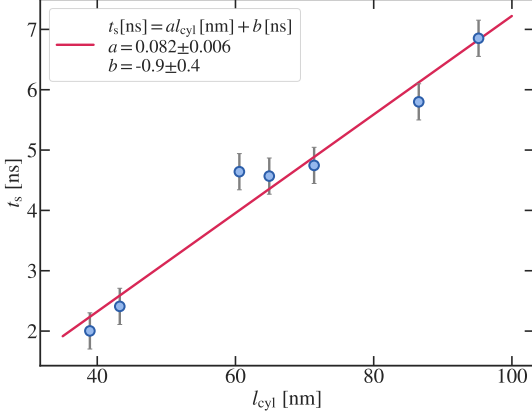
where $\beta = \left(\frac{M_{\text{C/F}} + m_n}{M_{\text{C/F}} - m_n} \right)^2$, and $M_{\text{C/F}}, m_n$ are the masses of carbon/fluorine nuclei and a neutron respectively. The values of β are approximately 0.7141 for ^{12}C and 0.8085 for ^{19}F . The differential solid angle is equal to $d\Omega = 4\pi\xi(E_n, \mathcal{T})d\mathcal{T}$, yielding $\frac{d\Omega}{d\mathcal{T}} = 4\pi\xi(E_n, \mathcal{T})$. The differential cross section with respect to \mathcal{T} then reads

$$\frac{d\tilde{\sigma}}{d\mathcal{T}}(E_n, \mathcal{T}) = 4\pi\xi(E_n, \mathcal{T}) \frac{d\tilde{\sigma}}{d\Omega}(E_n, \mathcal{T}). \quad (\text{E2})$$

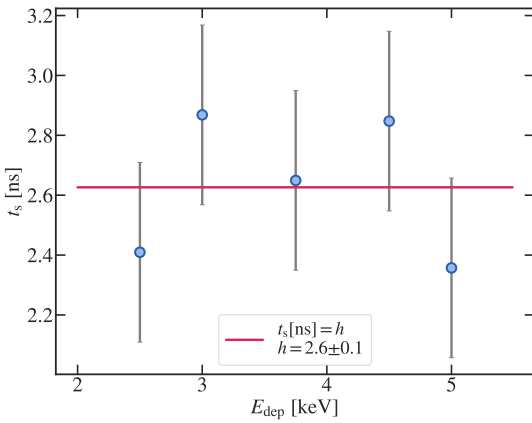
The dependence of the angular differential cross section, $\frac{d\tilde{\sigma}}{d\Omega}$, on \mathcal{T} comes from the link between \mathcal{T}, E_n , and the center-of-mass scattering angle θ_c :

$$\mathcal{T} = \frac{E_n}{2}(1 - \beta)(1 - \cos \theta_c). \quad (\text{E3})$$

The ENDF database [20] provides the measurements of $\frac{d\tilde{\sigma}}{d\Omega}(\theta_c)$ relations for a set of neutron energies E_n . Interpolating between these measurements at a 10 keV E_n resolution as in Fig. F.2, we can integrate the product of the fluence $\psi_n(E_n)$ and the differential cross section



(a) Dependence of t_s on the nucleus track length l_{cyl} for a fixed $\frac{E_{\text{dep}}}{l_{\text{cyl}}} = \frac{5 \text{ keV}}{4R_c} \approx 57.8 \frac{\text{keV}}{\mu\text{m}}$. We drop the $-0.9 \pm 0.4 \text{ ns}$ intercept as it will become less significant for larger track lengths.



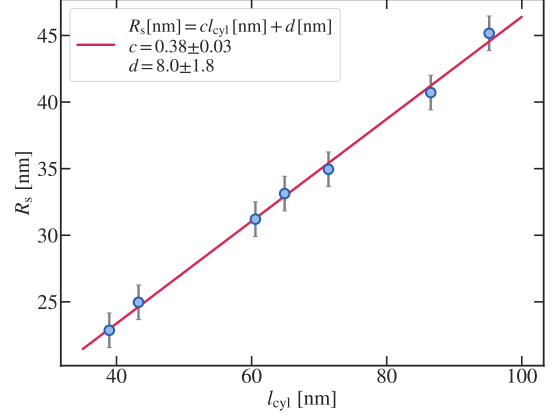
(b) Dependence of t_s on the energy E_{dep} deposited along fixed $l_{\text{cyl}} = 2R_c$.

FIG. D.2. Variation of the time t_s elapsed after the heat spike when the bubble eccentricity reaches its first minimum (see Fig. 2b) with the energy deposition parameters E_{dep} and l_{cyl} . The error bars represent the statistical uncertainty on t_s measured with different random seeds.

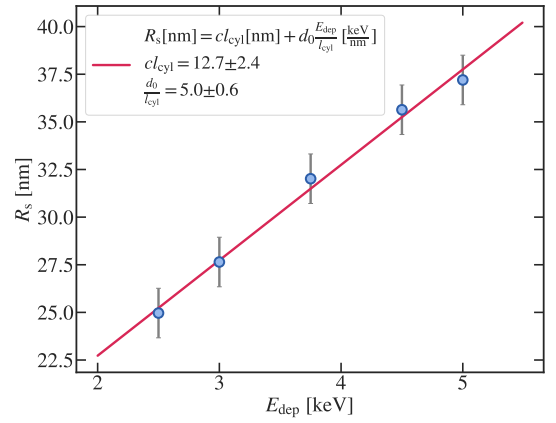
$\frac{d\tilde{\sigma}}{d\Omega}(\theta_c)$ to obtain the probability $\Pi(\mathcal{T}_i)$ of having a fluorine recoil energy between \mathcal{T}_i and $\mathcal{T}_{i+1} \equiv \mathcal{T}_i + \Delta\mathcal{T}$:

$$\Pi(\mathcal{T}_i) = \mathcal{N} \int_0^{E_n^{\text{max}}} \psi_n(E_n) \xi(E_n, \mathcal{T}_i) \frac{d\tilde{\sigma}}{d\Omega}(\mathcal{T}_i, E_n) dE_n, \quad (\text{E4})$$

where the factor \mathcal{N} is included to normalize the integrated probability density to 1.



(a) Dependence of R_s on the length of the energy deposition region l_{cyl} (see Fig. 2b) for a fixed $\frac{E_{\text{dep}}}{l_{\text{cyl}}} = \frac{5 \text{ keV}}{4R_c} \approx 57.8 \frac{\text{keV}}{\mu\text{m}}$.



(b) Dependence of R_s on the energy E_{dep} deposited along fixed $l_{\text{cyl}} = 2R_c$.

FIG. D.3. Variation of the effective bubble radius R_s at the first minimum in the bubble eccentricity (see Fig. 2b) with the energy deposition parameters E_{dep} and l_{cyl} . The error bars correspond to the statistical uncertainty on R_s measured with different random seeds and the systematic uncertainty equal to a half of the grid cell width ($2\sigma \approx 1 \text{ nm}$).

Appendix F: Tabulated data informing the AP distribution model

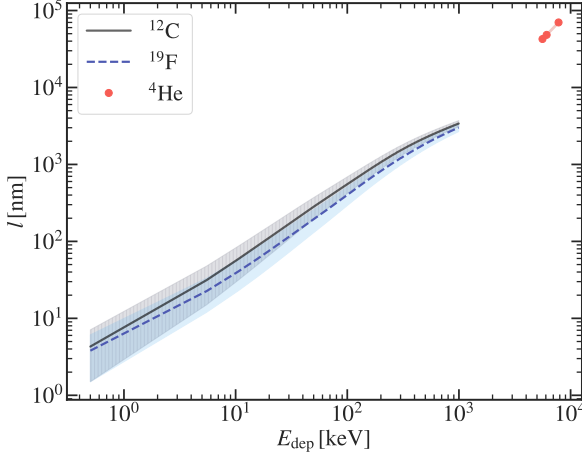


FIG. F.1. Ranges of ^{12}C , ^{19}F , and ^4He ions in C_3F_8 ($\rho_1 = 1379 \text{ kg m}^{-3}$) extracted from SRIM [17] and plotted as functions of their energies. For α particles, we consider the three energies released in the ^{222}Rn to ^{210}Pb decay chain (7). For C and F, a range of recoil energies from 0.5 to 1000.5 keV with a 5 keV step is assumed. The shaded areas correspond to the 1- σ longitudinal straggling of the nuclei due to collisions.

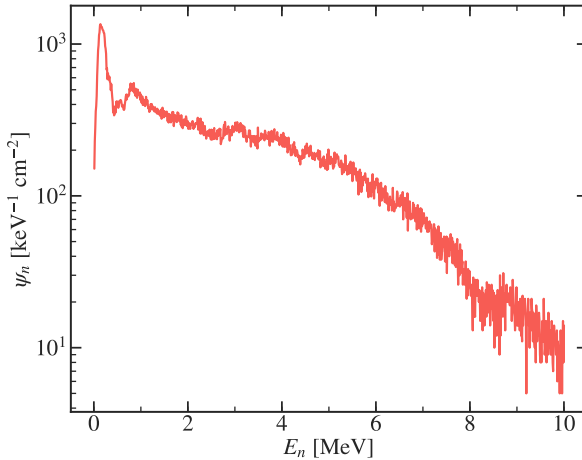


FIG. F.2. An arbitrarily normalized spectrum of $^{241}\text{Am}/^9\text{Be}$ source neutrons after propagation through the water tank in which the detector is mounted. Neutron energies are discretized at 10 keV resolution. Elastic scattering of these neutrons within the superheated C_3F_8 give rise to carbon and fluorine recoils according to Eq. E3.